Regional Grid Refinement in an Earth System Model: Impacts on the Simulated Greenland Surface Mass Balance

Leonardus van Kampenhout[1], Alan M. Rhoades[2], Adam R. Herrington[3], Colin M. Zarzycki[4], Jan T.M. Lenaerts[5], William J. Sacks[4], and Michiel R. van den Broeke[1]

[1]Institute for Marine and Atmospheric Research Utrecht, Utrecht University, The Netherlands
[2]Lawrence Berkeley National Laboratory, Berkeley CA, USA
[3]Stony Brook University, Stony Brook NY, USA
[4]National Center for Atmospheric Research, Boulder CO, USA
[5]Department of Atmospheric and Oceanic Sciences, University of Colorado, Boulder CO, USA

Correspondence: Leo van Kampenhout (L.vankampenhout@uu.nl)

Abstract. In this study, the resolution dependence of the simulated Greenland ice sheet surface mass balance in the variable-resolution Community Earth System Model (VR-CESM) is investigated. Coupled atmosphere-land simulations are performed on two regionally refined grids over Greenland at 0.5°(∼55 km) and 0.25° (∼28 km), maintaining a quasi-uniform resolution of 1°(∼111 km) over the rest of the globe. On the refined grids, the SMB in the accumulation zone is significantly improved compared to airborne radar and in-situ observations, with a general wetting at the margins and a drying in the interior GrIS. Total precipitation decreases with resolution, which is in line with best-available regional climate model results. In the ablation zone, CESM starts developing a positive SMB bias with increased resolution in some basins, notably in the east and the north. The mismatch in ablation is linked to changes in cloud cover in VR-CESM, and a cold bias that CESM has in these regions. Overall, our pilot study demonstrates that variable resolution is a viable new tool in the cryospheric sciences, and could e.g. be used to dynamically downscale SMB in scenarios simulations, or to force dynamical ice sheet models through the CESM coupling framework.

1 Introduction

The contribution of the Greenland ice sheet (GrIS) to global sea level rise is increasingly determined through its surface mass balance (SMB) (van den Broeke et al., 2016). Accurate estimates of future GrIS SMB are therefore key in providing projections for sea level rise. Arguably the most realistic SMB projections to date are derived from general circulation model (GCM) scenario output downscaled using regional climate models (RCMs — e.g., Rae et al. (2012); van Angelen et al. (2013); Fettweis et al. (2013a); Mottram et al. (2017); Noël et al. (2018)). Compared to GCMs, the regional models offer more sophisticated snow models that have improved representation of albedo, melt, firn densification and refreezing, features that are lacking in

most current GCMs (Ziemen et al., 2014; Helsen et al., 2017). In addition, RCMs typically run at a horizontal grid resolution of $\mathcal{O}$(10 km) whereas atmospheric GCMs are typically run using 1° or $\mathcal{O}$(100 km) grids. RCMs therefore tend to better resolve topographic gradients, which leads to more accurate spatio-temporal distributions in precipitation, wind, cloud cover, and temperature, enabling a detailed comparison to in-situ meteorological data. A fine spatial resolution seems indispensable for resolving narrow ablation zones found around the GrIS margins (Lefebre et al., 2005; Pollard, 2010).

Recently, significant efforts have been invested into making GCMs more suitable for snow and SMB modelling (e.g., Punge et al., 2012; Cullather et al., 2014; Fischer et al., 2014; Helsen et al., 2017; van Kampenhout et al., 2017; Shannon et al., 2019). In particular, improvements made to the Community Earth System Model (CESM) include a multilayer snow model with a two-way radiative transfer model for albedo (Flanner and Zender, 2005), enhanced snow density parameterizations (van Kampenhout et al., 2017), and the introduction of multiple elevation classes for downscaling SMB with height (Lipscomb et al., 2013). Still, significant biases remain with respect to RCMs, as the spatial resolution is limited (Vizcaíno et al., 2013; Helsen et al., 2017). Although high-resolution GCM simulations exist (50 km, Delworth et al. (2011); 25 km, Wehner et al. (2014); Small et al. (2014); Bacmeister et al. (2014); 80 km, Müller et al. (2018)) a majority of ongoing modelling experiments, notably the forthcoming CMIP6 experiments (Eyring et al., 2016), maintain a $\sim$1° atmosphere grid due to limitations in computational resources.

A middle road may be found in new techniques that apply regional grid refinement within a global climate model. In this approach, a static global mesh is constructed which has increased resolution over a specified region of interest. Over the past five years, progress has been made in developing regional grid refinement in CESM — variable resolution or VR-CESM. To date, studies looked at the effect of grid refinement on the global circulation and climatology (Zarzycki et al., 2015; Gettelman et al., 2018), the effect on tropical cyclones (Zarzycki and Jablonowski, 2014), regional climate in the presence of mountains (Rhoades et al., 2015; Huang et al., 2016; Rhoades et al., 2017), and the scale dependence of the underlying physics (Gettelman et al., 2018; Herrington and Reed, 2018). Compared to RCM downscaling, Huang et al. (2016) notes several advantages of the variable resolution (VR) approach. First, using a unified modelling framework avoids the inconsistencies between RCM and GCM, in particular the different dynamical core and physics that are used. Second, VR allows for two-way interactions (i.e., downstream / upstream effects) between the refinement region and the global domain, which an RCM downscaling approach does not. Finally, some more practical advantages are the attractiveness of operating a single modelling framework, and the relatively low computational cost associated with VR-CESM.

In this paper, we apply regional grid refinement over the Greenland area using VR-CESM, and explore the impacts that the refinement has on GrIS SMB. Two VR meshes are constructed with refined patches centered around the GrIS with 55 km and 28 km resolution, respectively. A 20-year atmosphere-only simulation spanning the historical period (1980-1999) is carried out over each of those grids and is then compared to a reference simulation that has no refinement. Results are also compared to reanalyses, airborne snow accumulation radar, in-situ SMB measurements, and gridded climate data from an RCM, in an ongoing effort to improve the representation of ice sheets in CESM (Lipscomb et al., 2013; Vizcaíno et al., 2013; Lenaerts et al., 2016; van Kampenhout et al., 2017). The version of CESM used resembles the recently released CESM version 2 (CESM2), of which a more in-depth evaluation will be published in the near future. The layout of the manuscript is as follows. In Section

2, the modelling setup and benchmark data are described in further detail. The main findings are presented in Section 3. A discussion follows in Section 4 that is concerned with interpreting an outstanding bias in CESM, not alleviated by the grid refinement, and guiding future research directions. Finally, a summary with conclusions is found in Section 5.

2 Methodology

2.1 Modelling setup

The Community Earth System Model (CESM) is a global climate modelling framework comprised of several components, i.e. atmosphere, ocean, land surface, sea ice, and land ice, that may operate partially or fully coupled. When partially coupled, the missing components can be substituted by external data or even inactive (stub) components. Here, we follow the protocol of the Atmospheric Model Intercomparison Project (AMIP, Gates et al. (1999)) and dynamically couple the atmosphere-land components and prescribe ocean and sea ice data at monthly intervals (Hurrell et al., 2008). Our three AMIP-style CESM simulations are carried out over the years 1980-1999, a period prior to the onset of persistent circulation change and a strong decline in GrIS SMB in the 2000s (Fettweis et al., 2013b; van den Broeke et al., 2016). Aerosol and trace gas emissions are taken as observed.

The atmosphere component used is the Community Atmosphere Model version 5.4 (CAM5.4, Neale et al., 2012) with the spectral element dynamical core (CAM-SE, Dennis et al., 2012; Lauritzen et al., 2018), the only dynamical core currently in CESM supporting VR capabilities (Zarzycki et al., 2014). VR capabilities in CAM6, the new atmosphere model in CESM version 2 (CESM2, www.cesm.ucar.edu/models/cesm2.0) were still under beta testing at the start of our study, which explains the slightly older model version of CAM. Our model configuration broadly follows that of Zarzycki and Jablonowski (2014), with a few modifications. These include updated rain and snowfall microphysics (MG2, Gettelman and Morrison (2014)), a new dry-mass, floating Lagrangian, vertical coordinate with 32 levels in the vertical, and slightly reduced horizontal diffusion in the SE dynamical core (Lauritzen et al., 2018). Further, we adopt the Beljaars et al. (2004) orographic drag parameterization which replaces the turbulent mountain stress (TMS) scheme of CESM1 (Neale et al., 2012) in order to achieve more realistic (higher) wind speeds over the ice sheets. Physics tuning coefficients were set to default values specified in the supported CAM5 release.

2.2 Grids

Our reference simulation, referred to as Uniform CESM, uses a standard cubed sphere grid which is quasi-uniform at 1° (∼111 km) resolution globally (Evans et al., 2012). The first non-uniform VR mesh has a refined patch of 0.5° (∼55 km) over the greater Greenland region and is referred to as VR-CESM55. The patch was constructed such that the boundary of the patch always extends at least six spectral elements away from the Greenland coast (Figure 1). This buffer region is intended to allow incoming "low-resolution" storms to develop finer-scale structures after entering the VR zone and prior to making landfall (Matte et al., 2017). The second VR mesh is constructed off the VR-CESM55 grid, yet features a second level of refinement at

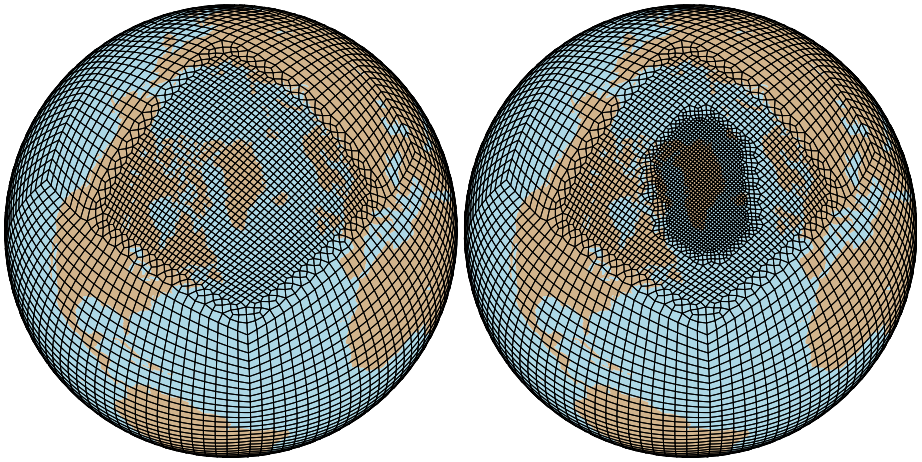

Figure 1. Computational domains of experiments VR-CESM55 (left) and VR-CESM28 (right). Each spectral element visible here contains an additional 3-by-3 grid of points, the exact position of which are determined by the spectral element method (Zarzycki and Jablonowski, 2014).

0.25° (∼28 km) inside the first level. This second patch was chosen such that, again, the boundary extends at least six spectral elements away from the Greenland coast. The simulation on this grid is referred to as VR-CESM28 and both VR grids were constructed using SQuadGen (Ullrich, 2014).

Topographic height over Greenland was interpolated from the 4 km CISM ice sheet domain, which in turn has been derived from the 90 m Greenland Ice Mapping Project product (GIMP, Howat et al. (2014)). Topography is static in time – ice sheet dynamics are not active in this configuration – a reasonable assumption for the decadal length simulations presented in this paper. The new ice topography was spliced into the global topography, similar to what is done in two-way coupled setups where ice sheet dynamics are turned on[1]. Due to the hybrid sigma vertical coordinate system implemented in CAM-SE, a differential smoothing procedure was applied to ensure numerical stability and realistic flow, as described by Zarzycki et al. (2015). Subgrid height variances, used by the orographic drag parameterization, are consistently recomputed as a residual of the smoothed topography.

The resulting GrIS topographies are shown in Figure 2, with a rendering of GIMP for comparison. As one would expect, a more detailed and accurate representation of topography is possible on finer resolutions. The feature most prominently improving is the southern ice dome, that "rises up" from ∼2300 m at 111 km to ∼2900 m at 28 km. Furthermore, the 28 km resolution seems sufficiently detailed to start resolving some of the fjord structures, especially in the east. The non-zero topographic heights over open ocean in Figure 2 are explained by the differential smoothing procedure.

The CAM physics (dynamics) time steps for Uniform CESM was 1800 (150) seconds. For the VR-CESM runs, the physics time step was set to 450 s and the CAM dynamics time steps scaled with horizontal resolution with VR-CESM55 at 150 s and

[1]For details, see the CESM Land Ice Documentation and User Guide, https://escomp.github.io/cism-docs/cism-in-cesm/versions/release-cesm2.0/html/clm-cism-coupling.html

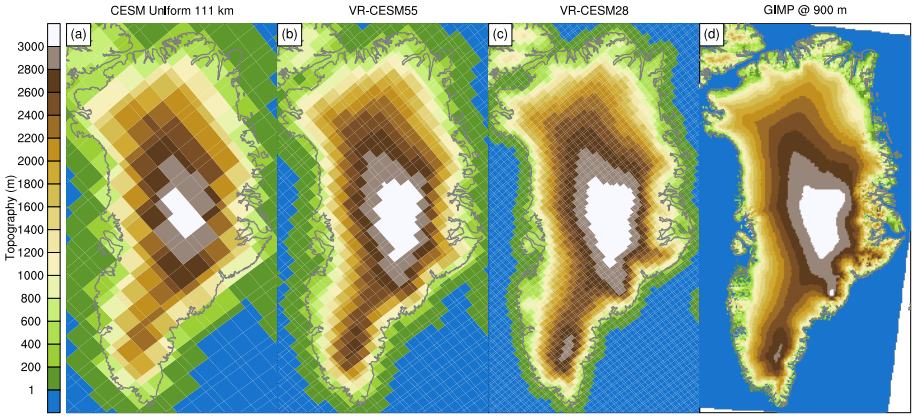

Figure 2. Topographic height in the three CESM simulations. For plotting purposes, spectral element node heights are displayed on control volumes equal to the area that they represent. The control volumes are identical to those used by the CESM coupler to conserve mass and energy. For reference, topographic height according to the Greenland Ice Mapping Project (GIMP, Howat et al. (2014)) is shown, which has been upscaled to 900 m.

VR-CESM28 at 75 s. Hyperviscosity coefficients are scaled by the grid-resolution (element dimensions) for numerical stability and filter undesirable numerical artifacts (Guba et al., 2014). Here the scaling is such that the hyperviscosity coefficients are reduced by an order of magnitude for each doubling of the resolution (Zarzycki and Jablonowski, 2014). Some minor grid imprinting was noted in the grid transition zone over distorted SE elements. It is deemed unlikely, however, that these small, local anomalies materially impact the large-scale synoptic flow in the interior of the domain.

2.3 Land surface model

CAM is coupled to the Community Land Model (CLM) version 5.0, which incorporates several important bug fixes and snow parameters updates for CESM2. CLM simulates the interaction of the atmosphere with the land surface, notably the surface energy balance and hydrological processes such as interception by canopy, throughfall, infiltration, and runoff (Oleson, 2013). For radiation calculations over snow, the two-way radiative transfer model SNICAR is used (Flanner and Zender, 2005). The snow pack hydrological and thermal evolution is modelled as a one-dimensional column, which can reach depths of up to 10 metres of w.e. (water-equivalent). Several snow model modifications have been implemented specifically for ice sheets, such as wind-dependent fresh snow density and wind driven snow compaction (van Kampenhout et al., 2017) and temperature dependent fresh snow grain size. Bare ice albedo is assumed constant, and is set to 0.50 (0.30) for the visible (near-infrared) spectrum, reflecting the distinction made between these two shortwave bands in CLM (Oleson, 2013).

Over glaciated grid cells, CLM maintains 10 different elevation classes in order to more accurately capture SMB gradients. Each elevation class is linked to an independent CLM column, and is given a weight proportional to the subgrid topography present in the CLM grid cell (Lipscomb et al., 2013). Classes with zero weights are considered "virtual" and do not contribute to the grid cell average. The columns are independent as they maintain their own private snow pack and ice / soil variables.

Columns tend to evolve differently depending on their height, as temperature, specific humidity and longwave radiation are downscaled to the mean class elevation. Lapse rates are used for temperature (6 K km^{-1}, Lipscomb et al. (2013)) and longwave radiation (32 W m^{-2} km^{-1}, based off Figure 6 in Van Tricht et al. (2016)), whereas specific humidity follows the assumption that relative humidity remains constant with height. Elevation classes have been shown to improve SMB gradients over Greenland (Vizcaíno et al., 2013). In order to activate elevation classes over Greenland, the Community Ice Sheet Model (CISM) must be active as a diagnostic component. SMB is the main focus of this paper. We deviate from the standard CLM definition of SMB, which does not take into account changes in snow pack height, in favour of the definition that is common to glaciology, in absence of redistribution/erosion by drifting snow

$$\mathrm{SMB} = \mathrm{Precipitation} - \mathrm{Sublimation} - \mathrm{Runoff}. \tag{1}$$

For the remainder of the paper, modelled accumulation (ablation) is defined as modelled SMB for locations where SMB > 0 (SMB < 0). Unless indicated otherwise, annual CESM SMB data used have been downscaled to the 4 km CISM ice sheet grid, thus taking advantage of the multiple elevation classes in CLM. In this downscaling procedure, elevation classes are used in the vertical direction whereas a bi-linear interpolation is applied in the horizontal direction to prevent artificial jumps between grid cells (Leguy et al., 2018).

Following Rhoades et al. (2018), the distribution of plant functional types in CLM is assumed constant at year 2000 values for all simulations. As the main focus of this work is on precipitation and snow cover in non-vegetated regions, we argue this assumption has a negligible impact on our results.

2.4 Initialisation

In glaciated regions, the subsurface conductive heat flux at the ice sheet surface is potentially large due to the high thermal conductivity of ice. To avoid unrealistic energy losses or gains from the subsurface, one should start with ice that is in thermal equilibrium with the ambient climate. In our modelling setup, however, a sufficiently long spinup period to achieve such equilibrium was not feasible due to computational constraints. Instead, it was decided to initialise deep ice temperature from values close to observed, in this case 10 m firn temperatures from a firn densification model, forced by RCM-downscaled reanalysis data (Ligtenberg et al., 2018). A nearest neighbour procedure was followed to interpolate ice temperature from the 11 km firn model to the different resolutions used in this study.

Snow height was reset globally to a low value of 100 mm w.e. to avoid snow cover hysteresis arising from errors in the interpolated initial conditions. This reset was limited to grid cells — or rather, CLM columns — below 1774 m, which is an estimate of the maximum present-day GrIS equilibrium line altitude. A spinup simulation was carried out to rebuild snow in any CLM columns residing below the reset altitude (1774 m) where the local climate dictates perennial snow cover. The relevance of this spinup is two-fold: (1) the dependence of fractional snow cover on snow height (Swenson and Lawrence, 2012), (2) the refreezing capacity of the snow pack. For both of these, a period of 5 years was deemed sufficiently long to capture the first-order effect. Nonetheless, it is recognised that the resulting snow depth distribution over the GrIS contains an artificial jump at 1774 m.

2.5 Performance

All simulations have been performed on NCAR's supercomputing facility "Cheyenne" in Wyoming, USA, which is equipped with Intel Broadwell processors. No real load-balancing was needed since the active components (i.e., CAM, CLM, CISM, and coupler) perform well when sharing all the available cores. On 1800 cores (or 50 compute nodes) the cost of Uniform CESM at 1° (48,602 CAM-SE grid points) amounts to ∼1070 core hours per simulated year. Keeping the number of cores the same, this cost was tripled to 3250 core hours for the VR-CESM55 simulation with the refined patch of 0.5° (59,402 CAM-SE grid points), and quadrupled to ∼4300 core hours for the VR-CESM28 simulation with the additional 0.25° patch (69,887 CAM-SE grid points). By comparison, the computational cost of limited area model RACMO2 at 11 km is ∼6800 core hours per simulated year (Brice Noël, pers. comm.). The throughput was ∼25, ∼13 and ∼10 simulated years per day for Uniform CESM, VR-CESM55 and VR-CESM28, respectively.

2.6 Reference data

Output from the three CESM simulations is interpreted using reference data from a variety of sources. The evaluation of the climate at synoptic scales is supported by atmospheric reanalyses, i.e. hindcast climate models that employ data assimilation to match the observed state of atmosphere as close as possible. In particular, temperature and geopotential height from the European Centre for Medium-Range Weather Forecasts Reanalysis (ERA-Interim, Dee et al. (2011)) and the Modern-Era Retrospective Analysis for Research and Applications-2 (MERRA2, Molod et al. (2015)) products are used.

For evaluation of GrIS near-surface climate and surface mass balance, data from the Royal Netherlands Meteorological Institute (KNMI) regional atmospheric climate model (RACMO) version 2.3p2 (RACMO2 hereafter) are used. RACMO2 is a state-of-the-art polar climate model that has been extensively evaluated over the GrIS (Noël et al., 2018, 2015) and compares favourably to observations. At its lateral boundaries, RACMO2 was forced using ERA-Interim data and the native spatial resolution of the data is 11 km. When appropriate, however, the statistically downscaled product at 1 km is used, which better resolves narrow ablation zones and low-lying regions (Noël et al., 2016, 2018). We argue that it is fair to compare VR-CESM directly to the downscaled 1 km RACMO2 product as (i) CESM also performs on-line downscaling using the semi-statistical elevation classes (Section 2.3), and (ii) best-estimate data is preferred in order to identify either model improvements or regressions, in line with the purpose of this paper. Still, these best-estimate benchmark data are subject to some uncertainty. Noël et al. (2018) characterise the native spatial resolution of 11 km as a source of model uncertainty, as well as the representation of surface roughness and surface albedo. Two prime uncertainties in the RACMO2 downscaling procedure arise from the bare ice albedo used to correct runoff, and the ice sheet extent (Noël et al., 2016).

Field data analysis has been carried out through the Land Ice Verification & Validation Toolkit (LIVVkit), an open source software package designed for evaluating ice sheet models and their forcing (Kennedy et al., 2017; Evans et al., 2018). Three observational SMB datasets available for the GrIS are used: (i) airborne radar, (ii) field accumulation (SMB > 0) measurements, and (iii) field ablation (SMB < 0) measurements (Evans et al., 2018). The airborne radar data stems from NASA's Operation IceBridge and covers most of the GrIS interior. The raw data, as described by Lewis et al. (2016), provides seasonal estimates

for a given pixel, uniquely determined by its latitude and longitude. Following Evans et al. (2018), a simple time average is applied over all available periods for each record to yield a single accumulation value (in mm w.e. yr^{-1}) per location. The resulting number of IceBridge data points is a sizeable 18,968, which means that the spatial density is quite high over the radar transects. During the evaluation, a nearest neighbour method is used to determine the model cell closest to each observation.

The in-situ field accumulation dataset is a compilation of different field campaigns carried out in the GrIS accumulation zone (Cogley, 2004; Bales et al., 2009; Evans et al., 2018). Only records that have been retrieved using firn cores, snow pits or stake measurements are included in the evaluation. Moreover, if there are multiple measurements at one location then the data is averaged in time to yield a climatological SMB estimate for that location. In total, the number of accumulation zone measurements is 421. The in-situ field ablation dataset is a subset of the compilation of GrIS ablation zone SMB measurements by Machguth et al. (2016). Again, each record location is averaged in time to yield an annual SMB estimate. Only records that are on the CISM ice mask and have a record length equal or close (i.e., within a 5% difference) to a full year are kept, which brings the total number of records down from 627 to 163, spread over 22 rather than 46 glaciers. It is important to mention at this point that the spatial coverage of the ablation zone measurements is quite sparse. Indeed, Figure 1 in Evans et al. (2018) illustrates that all in-situ ablation data stem from merely 8 transects in total.

3 Results

3.1 Large-scale circulation

We start with a comparison of modelled mid-troposphere climate to reanalyses data, which serves two purposes. First, it is useful to identify any significant climatic biases that CESM possesses, which could aid in interpreting e.g. snow melt rates later on. Second, the VR approach allows for feedbacks between the domain of interest and the global climate system, in contrast to dynamical downscaling using RCMs. One such feedback could be changes to the strength and location of planetary waves both in and outside the VR domain, due to the higher and steeper topography (Figures 1 and 2). If such upstream / downstream dynamical effects are present in our modelling setup they would make an imprint on mid-tropospheric climate on a hemispheric scale.

CESM geopotential height (Z500) at 500 hPa is compared against ERA-Interim over the period 1980-1999. Note that the choice of ERA-Interim versus MERRA-2 does not impact our results much, so only ERA-Interim is shown. In boreal summer, the season most relevant to GrIS SMB, anomaly maps of Z500 display consistent patterns across all three CESM simulations (Figure 3a-c). A positive height anomaly is found over the Arctic ocean, which is most pronounced in the Uniform CESM 111 km simulation. It is surrounded by a band of negative height anomalies in all three simulations, with one of the maxima approximately centred over Iceland / South Greenland, indicating more cyclonic flow over the GrIS in CESM. At mid-latitudes, positive height anomalies are found instead, indicating more anti-cyclonic flow there. Over the region 55-90N, the Z500 root mean squared error (RMSE) is decreased from 3.6 dam (Uniform CESM) to 3.5 dam (-2%, VR-CESM55) and 3.3 dam (-8%, VR-CESM28), which could signal minor benefits of the grid refinement on resolving the large-scale circulation. However, no VR-CESM grid point within the domain of interest can be significantly differentiated from Uniform CESM ($p < 0.05$, indicated

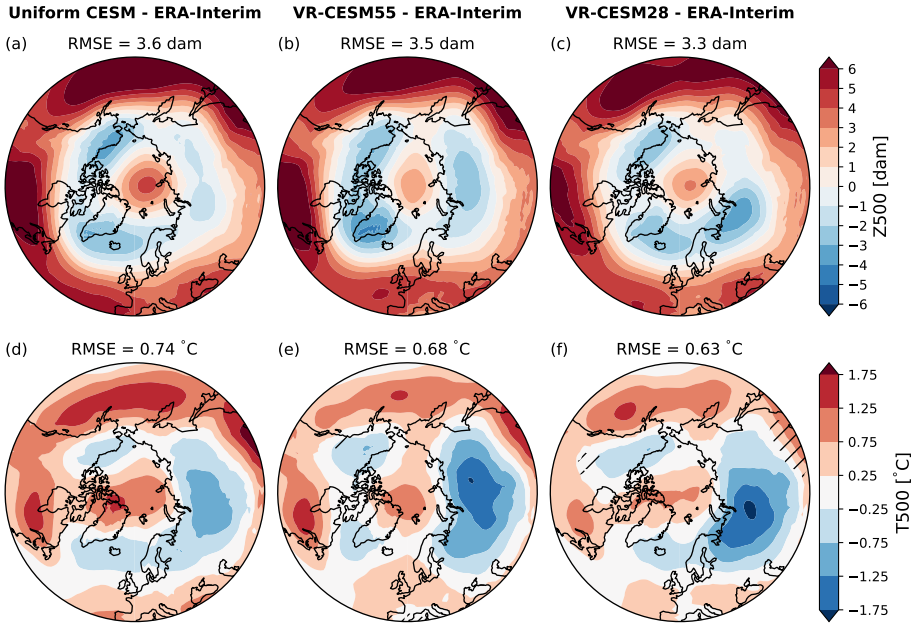

Figure 3. Mean summer (JJA) anomalies of 500 hPa geopotential height (Z500, panels a-c) and air temperature (T500, panels d-f) with respect to ERA-Interim over the period 1980-1999. Shown is 55-90N, the same region over which the area-weighted RMSE was calculated that is listed above each panel. VR-CESM simulations are significantly different ($p < 0.05$) from Uniform CESM in the hatched areas (panels b,c,e,f). Note that no significance is found in panels b, c, and e. Prior to subtraction, all data have been regridded to a common regular mesh of 1° using bi-linear interpolation.

by hatching in Figure 3b-c). Furthermore, similar decreases in RMSE are not evident in the other three seasons (Figures S1-S3, Supplementary Material) so these changes can be attributed to internal variability.

Similarly, anomalies of 500 hPa air temperature (T500) with respect to ERA-Interim are computed (Figure 3d-f). Major features in T500 are again shared by the three simulations, such as a cold bias exceeding 0.75 °C over Russia, which is most pronounced in VR-CESM55 and VR-CESM28. A slight JJA warm bias of around 0.5 - 1 °C is indicated over the Arctic Ocean and Northern Greenland in all three simulations. Over the region 55-90N, RMSE is decreased from 0.74 °C (Uniform CESM) to 0.68 °C (-8%, VR-CESM55) and 0.63 °C (-14 %, VR-CESM28). Similar improvements are found in MAM (Figure S1) but not in the other two seasons (Figures S2 and S3). Some point-by-point significance is found between VR-CESM and Uniform, albeit not over the Greenland area (Figure 3d-f).

To conclude, heights at 500 hPa seem not substantially affected by the enhanced resolution and topography in VR-CESM, in particular over the area of interest (Greenland). In all three CESM simulations, more cyclonic flow is indicated with respect to ERA-Interim. Temperature at 500 hPa demonstrates a weakly positive bias in CESM, and shows no significant change with refinement over the GrIS. A weak signal cannot be excluded, however, as it may remain undetected by the Student's t-test due to the relatively short sample period of 20 years.

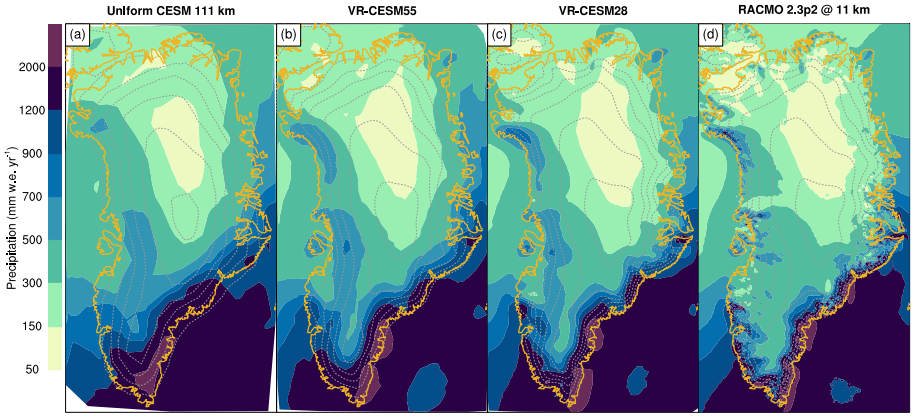

Figure 4. Spatial distribution of mean annual precipitation over Greenland. CESM data are displayed at the native CAM resolution for the period 1980-1999. RACMO2 data are shown at native 11 km resolution for the same period. Coastlines and 500 m elevation contours are overlain in orange and grey, respectively. Note the non-linear colour scale.

3.2 Precipitation

Both the steep edges of ice sheets as well as topographic promontories are effective drivers of orographic precipitation, as is e.g. apparent from the RACMO2 precipitation field (Figure 4d). The largest source of moisture is the North Atlantic basin, which is connected to Greenland by large-scale storm systems (Sodemann et al., 2008). Cyclonic activity associated with the persistent Icelandic Low drives warm and moist air onto land from the south-east, resulting in strong orographic uplift which causes rapid cooling, condensation, and precipitation. By comparison, northern Greenland is much drier with accumulation rates locally below 150 mm yr^{-1} (Cogley, 2004).

Since orographic precipitation is so dominant over southern Greenland, it is not surprising that we find significant improvements with increasing resolution (Figure 4), compared with RACMO2. At uniform 111 km resolution, CESM correctly predicts a band of high (> 1000 mm yr^{-1}) precipitation rates in the south-east, however it extends too far into the interior (Figure 4a). This is attributed to the fact that the poorly resolved topography is ∼600 m lower in the model than in reality (Figure 2a) and that topographic gradients are smoothed out, which weakens the effect of orographic uplift. The VR-CESM55 result (Figure 4b) shows that this is mostly a resolution issue as the band of high precipitation rates is more confined to the low-lying areas and slopes, similar to RACMO2. Other effects that can be seen in this VR-CESM55 result are the emergence of orographic precipitation in other locations around the margins, albeit weak, and a general drying of the northern interior. In VR-CESM28, similar resolution dependent patterns continue to emerge, with even stronger orographic precipitation and more pronounced drying in the north (Figure 4c). Integrated over the entire GrIS, including peripheral glaciers and ice caps, precipitation is reduced from 946 ± 107 Gt yr^{-1} (Uniform CESM) to 870 ± 72 (VR-CESM55) and 821 ± 62 Gt yr^{-1} (VR-CESM28). By comparison, RACMO2 simulates a mean annual precipitation flux of 743 ± 64 Gt yr^{-1} over these glaciated areas. Both the

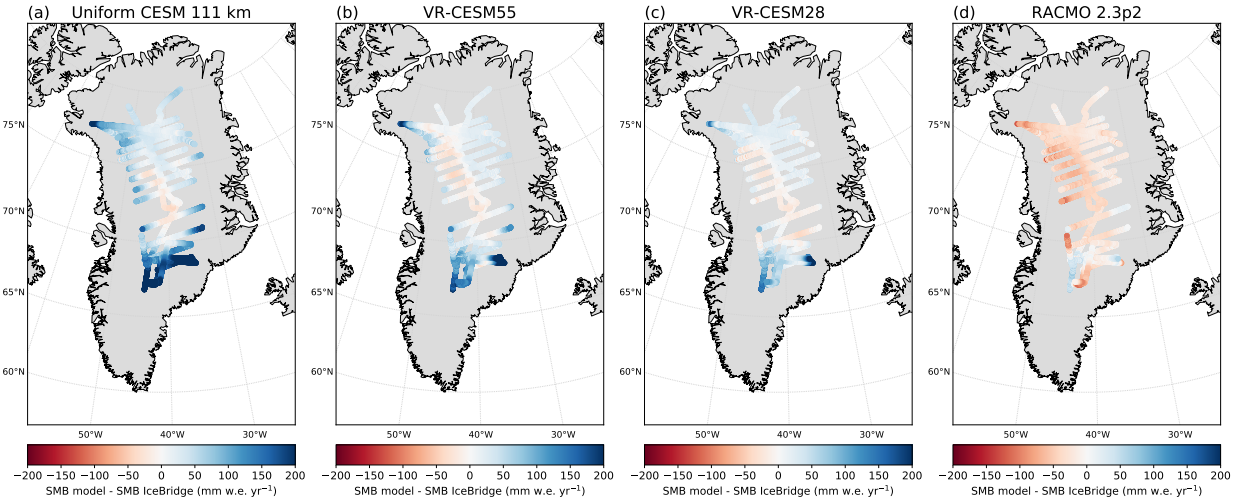

Figure 5. SMB differences between IceBridge radar (mean over available period) and model climatology (1980-1999). Blue (red) colours indicate that the model is wetter (dryer) than observations.

improved patterns (Figure 4) and the more reasonable integrated amount of precipitation over the GrIS are positive results for the application of VR-CESM to this region.

3.3 IceBridge

Operation IceBridge accumulation data is used to further quantify the effect of the improved precipitation patterns on SMB. As described in Section 2.3, CESM SMB is downscaled to 4 km using the elevation classes method and averaged over the period 1980-1999, prior to comparison to the processed IceBridge SMB samples (Section 2.6). Figure 5 displays the resulting SMB anomalies in mm w.e. yr^{-1}. As can be seen, the IceBridge radar data support the pattern of interior drying with increasing resolution. In Uniform CESM at 111 km resolution, we find a mean wet bias of 81 mm yr^{-1} which is most pronounced in regions near the edges of the IceBridge domain (Figure 5a). The strongest bias is found in the south, where absolute precipitation rates are highest (Figure 4) and any relative error will consequently lead to a larger absolute error. With increasing resolution, the mean bias drops from 81 mm to 37 mm (VR-CESM55) and 24 mm (VR-CESM28), which suggests that the largest improvement is made going from 111 km to 55 km (Figure 1). The largest SMB differences remain to be found near the margins of the IceBridge domain (Figure 5b-c). The spread in SMB anomaly also decreases with resolution, which can be visually seen as a narrowing of the SMB anomaly distribution in Figure 6a. As a measure for this spread, the difference between the 95th percentile and the 5th percentile falls from 308 mm (Uniform CESM) to 178 mm (VR-CESM55) and 115 mm (VR-CESM28), respectively. As another measure, the RMSE decreases from 126 mm (Uniform CESM) to 68 mm (-46%, VR-CESM55) and 46 mm (-64%, VR-CESM28). At the same time, the coefficient of determination (r^2) is enhanced substantially (Table 1). The bias and RMSE of the regional RACMO2 are -25 mm and 38 mm, respectively, which suggests a dry bias in RACMO2 (Figure 5d). We conclude that based these statistics, VR-CESM28 performs on-par with RACMO2 (Table 1).

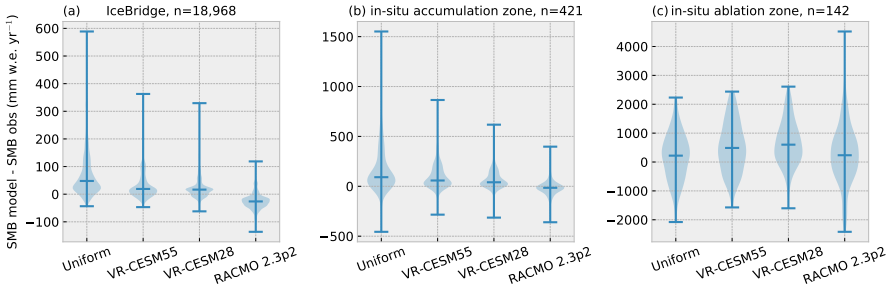

Figure 6. Distribution of point-by-point SMB differences between model and reference observations. Horizontal line segments indicate maximum, median, and minimum value. Model climatologies have been computed over the period 1980-1999.

Table 1. Selected statistics of CESM climatological SMB (downscaled to 4 km) and RACMO2 climatological SMB (downscaled to 1 km) with respect to IceBridge radar data, accumulation zone sites, and ablation zone sites. Shown are mean bias, coefficient of determination, and root mean square error. Model climatologies have been computed over the period 1980-1999, which not necessarily overlaps with the date of each measurement.

	IceBridge ($n = 18,968$)			Acc. sites ($n = 421$)			Abl. sites ($n = 163$)		
	bias (mm)	r^2	RMSE (mm)	bias (mm)	r^2	RMSE (mm)	bias (mm)	r^2	RMSE (mm)
Uniform CESM 1°	81	0.78	126	187	0.61	319	170	0.71	793
VR-CESM55	37	0.88	68	105	0.74	172	462	0.69	941
VR-CESM28	24	0.92	46	71	0.79	124	600	0.72	951
RACMO 2.3p2	-25	0.94	38	-13	0.71	91	160	0.54	922

3.4 Accumulation sites

A similar analysis is carried out for the in-situ accumulation zone observations. Compared to the airborne radar data, these measurements cover a greater portion of the GrIS, including the southern dome (cf. Figure 1 in Evans et al., 2018), which should make it more representative of the GrIS as a whole. As before, the greatest absolute improvement is found in the doubling of resolution from 111 km to 55 km, with smaller benefits going further to 28 km (Figure 6b and Table 1). The mean bias substantially reduces from 187 mm (Uniform CESM) to 105 mm (-44%, VR-CESM55) and 71 mm (-62%, VR-CESM28) and the RMSE reduces from 319 mm (Uniform CESM) to 172 mm (-46%, VR-CESM55) and 124 (-61%, VR-CESM28). A small positive accumulation bias remains even in the highest resolution run (VR-CESM28), a bias that is not apparent in the RACMO2 data (Table 1). For RACMO2, the bias and RMSE values are similar to those mentioned by Noël et al. (2018), who report in their Figure 11a an accumulation zone mean bias of -22 mm (here: -13 mm) and an RMSE of 72 mm (here: 91 mm). Our r^2 is slightly lower, however, 0.71 against 0.85. These differences can be explained by the different methodology used. Namely, Noël et al. (2018) correlate SMB values based off daily data, thus reflecting the meteorological conditions during

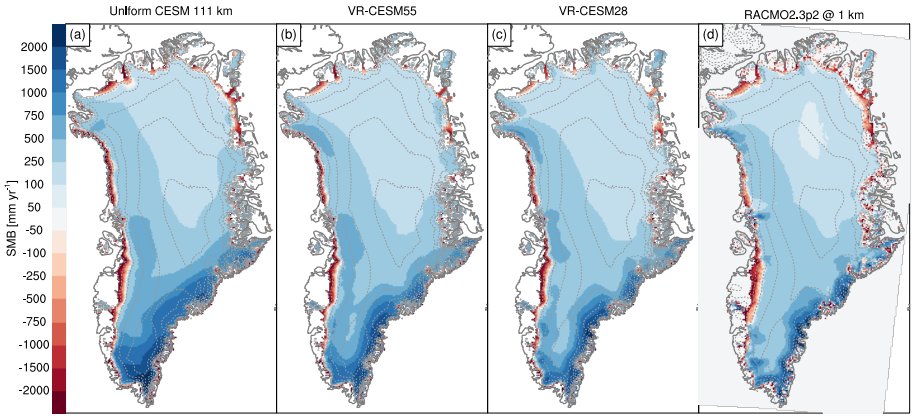

Figure 7. Mean annual SMB in mm yr^{-1}. All CESM data are downscaled to 4 km CISM resolution for the period 1980-1999. RACMO2 data have been statistically downscaled from 11 to 1 km. Note the non-linear colour scale.

which the measurement was made, whereas here we compare climatological averages of the model to each measurement, which introduces additional noise in the comparison.

3.5 Ablation sites

High up on the ice sheet, and thus deep into the accumulation zone, SMB is dominated by snowfall. In the ablation zone, by contrast, there is a delicate balance between different factors — snowfall, sublimation, snowmelt, refreezing, and runoff — that complicates SMB modelling. Furthermore, SMB gradients are typically much stronger in the ablation zone than they are in the accumulation zone, mainly due to steep topography and non-linearity of SMB with height (Figure 7). Therefore, as one expects, model skill in the ablation zone is lower than in the accumulation zone, signalled by a larger spread and modelling biases exceeding 1000 mm at many locations (Figure 6c). Nonetheless, ablation zones are mostly predicted in the right locations (Figure 7), owing to the elevation class subgrid parameterization described in Section 2.3.

In contrast to the accumulation zone and somewhat surprisingly, model skill in the ablation zone does not improve with resolution (Table 1). The mean bias grows from 170 mm (Uniform CESM) to 462 mm (VR-CESM55) and 600 mm (VR-CESM28), which are substantial increases of +172% and +253%, respectively. The model spread is only marginally detoriated, and RMSE ranges 793 - 951 mm for all simulations (Table 1). The ablation statistics of the overall best simulation (Uniform CESM) are comparable to those of RACMO2 which are, analogous to CESM, computed using a 1980-1999 climatology. The bias, r^2, and RMSE of RACMO2 are considerably worse than those reported by Noël et al. (2018), who find a bias of 120 mm (here: 160 mm), an r^2 of 0.72 (here: 0.54), and RMSE of 870 mm (here: 922 mm) in their ablation zone comparison with similar data (their Figure 11c). Again, this is explained by the different methodology used. In particular, we believe that some extreme ablation events that happened after the year 2000 are not well captured by the climatological mean of the two 20th century decades considered here. When the period of the RACMO2 climatology is changed to 1995-2017, we find a bias of -9 mm, an r^2 of 0.69, and RMSE of 722 mm, which confirms that the time frame used is a crucial factor. Overall, we conclude

Table 2. Mean GrIS mass fluxes for the period 1980-1999 in gigatonnes per year with standard deviation between brackets. The area of integration is listed in the first column and includes peripheral glaciers and ice caps (GIC). CESM data are integrated at the native resolution with elevation class weighing. The statistically downscaled 1 km RACMO2.3p2 data is averaged over the same period and described in Noël et al. (2018). RACMO2 does not differentiate between snow and ice melt in its output files so only total melt is reported.

Model name	Ice area km^2	Precipitation Gt yr^{-1}	Ice melt Gt yr^{-1}	Total melt Gt yr^{-1}	Refreezing Gt yr^{-1}	Runoff Gt yr^{-1}	Sublimation Gt yr^{-1}	SMB Gt yr^{-1}
	native ice sheet extent, including GIC							
Uniform CESM 1°	1,812,467	946 (107)	217 (48)	468 (100)	178 (43)	349 (67)	28 (3)	567 (129)
VR-CESM55	1,812,254	870 (72)	146 (25)	387 (70)	185 (39)	260 (42)	39 (3)	571 (75)
VR-CESM28	1,812,254	821 (62)	131 (34)	377 (73)	195 (35)	239 (47)	44 (2)	538 (87)
RACMO2	1,761,475	743 (64)	-	577 (81)	309 (27)	344 (68)	33 (2)	365 (109)
	contiguous GrIS extent							
Uniform CESM 1°	1,705,508	893 (104)	157 (37)	361 (85)	150 (40)	258 (53)	26 (3)	610 (116)
VR-CESM55	1,692,629	796 (69)	115 (20)	314 (62)	159 (37)	203 (34)	36 (3)	557 (71)
VR-CESM28	1,697,054	745 (59)	105 (28)	304 (63)	165 (33)	184 (38)	40 (2)	521 (77)
RACMO2	1,700,772	707 (61)	-	509 (72)	263 (25)	298 (58)	32 (2)	376 (99)

that both VR-CESM55 and VR-CESM28, despite their higher resolution over the GrIS, fail to recover in-situ ablation rates with a skill similar or better than the reference simulation. Instead, a strong positive SMB bias develops in some ablation zone sites, suggesting too little runoff and/or too much precipitation in these locations.

3.6 Integrated SMB

All major surface mass balance components are now integrated over the ice mask native to each model, as well as a common ice mask. Compared to RCMs, which are strongly forced by atmospheric reanalyses, our AMIP-style simulations experience relatively weak forcing at the ocean boundaries, which renders it unlikely that the actual historical Greenland weather conditions are reasonably resolved. Furthermore, a 20-year model simulation is arguably not long enough to attain a robust mean climate. Hence, the numbers presented in Table 2 should be interpreted with some caution, as RACMO2 and CESM are not necessarily experiencing the same climate. The common ice mask is constructed based on the contiguous GrIS definition, as laid out by the PROMICE mapping project (Citterio and Ahlstrøm, 2013), which is bilinearly upscaled from the 1 km RACMO domain to the respective CESM grids. In the remainder of this section, we will focus on the results that were obtained on the common ice mask.

GrIS-integrated precipitation is overestimated in all CESM simulations with respect to the RACMO2 regional model (Table 2). The bias in precipitation is largest for Uniform CESM (+186 Gt yr^{-1}, or +26 %) and reduces with increasing resolution to +89 Gt (+13%, VR-CESM55) and +38 Gt (+5%, VR-CESM28). This is in line with our earlier findings of progressive drying with increased resolution discussed in Sections 3.2, 3.3, and 3.4. Melt, on the other hand, is consequently underestimated in

all CESM simulations (Table 2). The bias in total melt volume is smallest for coarse-resolution Uniform CESM (-148 Gt, or -29%) and largest for fine-resolution run VR-CESM28 (-205 Gt, or -40%). Melt is reduced by 47 Gt in VR-CESM55 and by 57 Gt in VR-CESM28, with respect to Uniform CESM. The majority of that is due to ice melt, which sees similar reductions of 42 Gt and 52 Gt, respectively (Table 2), with snow melt accounting for the remainder of 5 Gt in both cases. Refreezing volume is comparable across the three different CESM simulations (Table 2), with only slightly higher numbers at higher resolution. These could be explained, for instance, by lower snow temperatures (“cold content") in these runs, which is consistent with the lower melt rates found. Surface runoff in CESM is the sum of bare ice melt and drainage from the bottom of the snow pack, i.e. liquid water originating from rain or melt that does not refreeze. Due to the reductions in total melt volume, runoff is also significantly reduced at higher resolutions (Table 2), leading to significant negative biases when compared against the downscaled 1 km RACMO2 data. With respect to RACMO2, Uniform CESM underestimates runoff by 40 Gt (-13%), VR-CESM55 by 95 Gt (-32%), and VR-CESM28 by 114 Gt (-38%), which agrees with the reduction in ablation found in Section 3.5. Sublimation is enhanced in both VR runs compared to Uniform CESM (Table 2) which we attribute to higher 10 m wind speeds occurring in VR-CESM (not shown). GrIS sublimation in VR-CESM28 is 54 % higher than in Uniform CESM, and exceeds the RACMO2 figure by 8 Gt.

Overall, GrIS integrated SMB exceeds 500 Gt in all CESM simulations (Table 2), which is markedly more than the 376 $\pm$ 99 that RACMO2 estimates over the common mask. There appear to be two balancing factors. On one hand, precipitation is overestimated in all CESM runs, and more so in the runs at low resolution (Uniform CESM and VR-CESM55). On the other hand, runoff is underestimated in all CESM runs, and more so in the runs at high resolution (VR-CESM55 and VR-CESM28). However, the decrease in precipitation is larger than decrease in runoff, which makes that the lowest integrated SMB value is found in VR-CESM28 (521 $\pm$ 77 Gt yr^{-1}).

3.7 Runoff

The decreased integrated runoff found in both VR-CESM simulations is an unexpected regression with respect to the uniform resolution simulation, and may be linked to a similar regression in reproducing ablation zone measurements (Section 3.5). It is interesting to examing the spatial heterogeneity of runoff, and uncover any regional differences. To this end, runoff is aggregated over 7 major GrIS drainage basins, derived from an ice flow mosaic updated from Rignot and Mouginot (2012). Downscaled RACMO2 runoff at 1 km is used as a reference and the results are shown in Figure 8. Clearly, Uniform CESM underestimates mean runoff in basin 1 (north), basin 2 (north-east), and basin 3 (east). In both VR runs, runoff decreases further in these regions and now falls completely outside of the standard deviation of RACMO2. In basin 4 (south-east), runoff is substantially overestimated in Uniform CESM (Figure 8). This can be explained through the poorly resolved precipitation field in Uniform CESM. In reality, precipitation has steep gradients over this basin that are not resolved due to the coarse resolution (Figure 4). In both VR runs, precipitation shifts to lower elevations, which enhances meltwater buffering / refreezing and prevents bare ice exposure, two mechanisms through which runoff can be limited. Indeed, VR-CESM55 runoff now falls within one RACMO2 standard deviation in basin 4, which is a positive result for this simulation, whereas VR-CESM28 runoff is slightly lower than RACMO2. The largest absolute runoff flux is found in basin 5 (south-west), which is equally well resolved

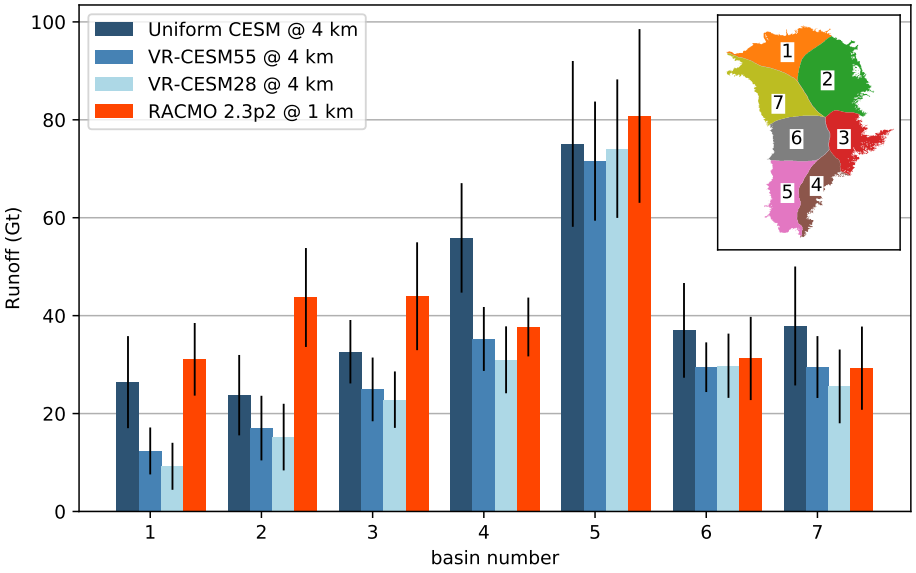

Figure 8. Mean basin-integrated runoff over the period 1980-1999. Error bars represent one standard deviation. CESM data have been manually downscaled down from their native resolution to 4 km using vertical SMB profiles generated by the elevation classes. For reference, RACMO2 downscaled runoff at 1 km resolution is shown. The extent of all basins combined equals the common ice mask in Table 2. Due to the manual interpolation, however, the total runoff for CESM does not match the value reported in Table 2.

by all CESM simulations, with numbers that fall within one standard deviation of the RACMO2 estimate. Finally, runoff in basin 6 (west) and basin 7 (north-west) is slightly overestimated in Uniform CESM, a bias that appears to be removed in both VR runs. In summary, our basin analysis indicates that runoff is particularly biased in the north, north-east, and east basins of the GrIS, and that this bias grows stronger with increasing resolution. In the other basins, VR-CESM runoff seems not substantially biased with respect to RACMO2.

3.8 Clouds

What could be causing the observed reduction in runoff, especially pronounced in the northern and eastern basins? Here, we aim to shed some light on that, in a qualitative fashion. Likely, large-scale circulation changes can be excluded as the prime driving mechanism, based on the results presented in Section 3.1. In particular, no statistically significant changes in Z500 and T500 were found over the Greenland area in summer (Figure 3). The same holds true when the lower troposphere is inspected at the 700 hPa pressure level (Figure S4, Supplementary Material), although some cooling is observed over northern Greenland, but this may include a thermodynamic effect of a cooler surface.

This leaves local meteorological conditions as the prime candidate mechanism. Clouds in particular are an important modulator of the surface energy balance, with thick clouds emitting more longwave radiation towards the surface and blocking incoming shortwave radiation. Here we present our model results of cloud presence and surface radiation, with a focus on

north and east Greenland during summertime, when runoff rates are typically largest. To inter-compare meteorological and surface conditions across the different CESM simulations, output from the atmosphere model CAM has been bilinearly re-gridded to a common 0.25° mesh. The anomalies thus computed (Figure 9) should be interpreted with caution since they incorporate interpolations errors. Nevertheless, these spatial anomaly plots may provide us with useful qualitative leads on some of the first order changes taking place in the VR refined simulations.

Figure 9a shows VR-CESM surface elevation anomalies with respect to Uniform CESM. The patterns are very similar in both VR-CESM55 and VR-CESM28, with lower surface topography over the ocean and near the margins of the island, and with higher surface elevations inland. As discussed previously, these features are explained by the smoothing operator applied by CAM to the topography, the imprint of which is much wider at low resolution than it is at high resolution (cf. Figure 2). Due to the higher and steeper terrain near the margins, orographic uplift and condensation are enhanced leading to increased cloud water path (CWP), the vertically integrated mass of liquid water and solid ice contained in clouds. Higher on the ice sheet, CWP decreases, as illustrated by Figure 9b. Some exceptions to this pattern exist, e.g. in north-east Greenland where CWP is locally reduced over the margin and ocean as well. Either changes in meso-scale flow driven by local topography, or increased katabatic surface winds (not shown) are possible explanations for this.

Downwelling longwave radiation is to some extent governed by CWP, which is apparent from Figure 9c, which resembles closely the cloud patterns (Figure 9b). As a result, negative longwave radiation anomalies are found nearly everywhere across the GrIS, with anomalies exceeding -10 W m^{-2} in the north and the east. Some areas where cloud water path has increased strongly (e.g. the patch far north) are not matched by strong positive longwave anomalies. This may be explained as a saturation effect at this particular location, while the slightly reduced lower troposphere temperature cannot be excluded as well (Figure S4). The reduced thermal flux exhibits a broad correlation to the ice sheet skin temperature (Figure 9d), which indicates a general cooling across the GrIS interior and strong negative anomalies in locations with reduced longwave. Some marked positive temperature anomalies are seen as well, which we interpret as a better resolved tundra region, with fewer grid cells having mixed land surface types of glacier and bare land. This is relevant since the skin temperature of the "glacier" land surface type never exceeds the freezing point (Oleson, 2013), whereas the tundra land surface type does in summer.

Importantly, meteorological conditions in all of the CESM simulation are inadequate to support a snow-free tundra in north Greenland during summer (Figure S5, Supplementary Material), despite the snow height reset to an extremely low value at the time of initialization (see Section 2.4). Snow buildup over the northern tundras is a known model bias in this version of CESM and our results suggest that this bias worsens, rather than improves, on VR refined grids. This is reflected in the albedo difference maps (Figure 9e) which shows that both VR simulations predict higher JJA albedo than the uniform resolution run. Albedo anomalies exceed 0.1 over much of north Greenland. As a result, significantly less shortwave radiation is absorbed which acts as a positive feedback sustaining the snow cover. In effect, the net radiation budget is negative over the entire north Greenland region (Figure 9f); this radiation deficit is partially offset by an enhanced sensible heat flux in both VR runs (not shown), which is however insufficient to prevent a net energy loss at the surface, i.e. the sum of all surface radiative and turbulent fluxes is negative. Note that albedo is also higher over the adjacent sea ice (Figure 9e). In fact, JJA sea ice albedo is found to increase over the entire Arctic basin (not shown), which appears linked to precipitation phase and frequency.

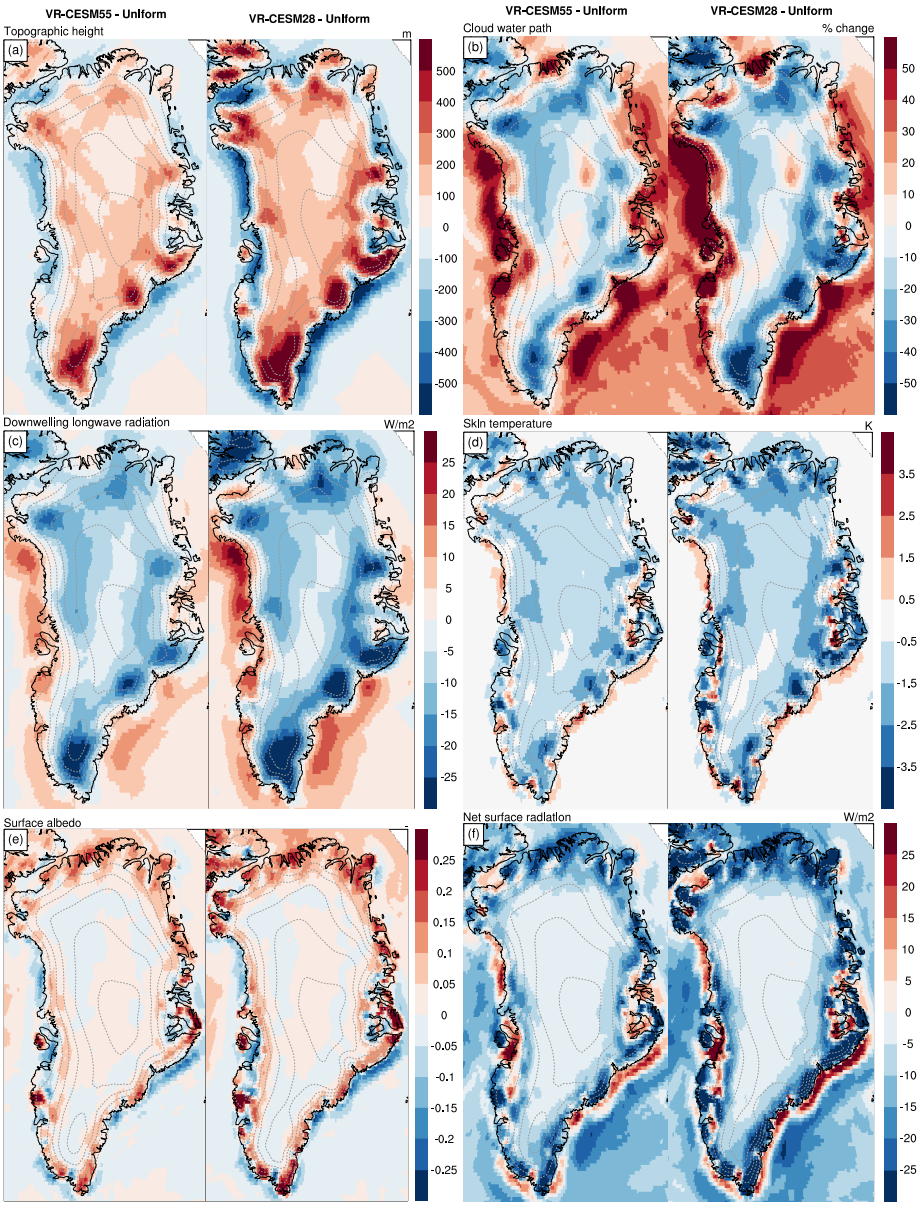

Figure 9. Summer (JJA) anomalies of atmospheric variables over the period 1980-1999, relative to the coarse resolution reference simulation (Uniform CESM). Panel (a) topographic height [m], (b) cloud water path [% change], (c) downwelling longwave radiation at the surface [W m^{-2}], (d) skin temperature [K], (e) surface albedo [fraction], (f) net radiation at the surface [W m^{-2}]. Prior to subtraction, all data have been regridded to a common regular mesh of 0.25° using bi-linear interpolation.

To summarize, a changed cloud distribution is proposed as the key mechanism that could explain the lower ablation rates in VR-CESM, relative to Uniform CESM. In particular, reduced cloud water paths are found across large stretches in the

northern and eastern regions of the GrIS leading to less heating of the surface. As a result, VR-CESM simulates a lower skin temperature in those regions, which is at least partly due to the reduction in longwave radiation, as the two variables broadly correlate. At the same time, CESM fails to simulate a seasonal snow cover over the northern tundras in all simulations, thereby reinforcing the cold bias that this region experiences, through albedo. The reduced ablation rates in VR-CESM are explained by the negative net radiation anomalies seen in these simulations.

4 Discussion

All of our CESM runs are simulating a perennial snow cover over the North Greenland tundra, or at least partly (Figure S5, Supplementary Material). In reality, these tundras and the adjacent bare ice zones do experience a seasonal snow cover. This is a delicate balance, however, with little snowfall (cf. Figure 4) and a relatively short melt season, that could tip towards the positive side without much difficulty. Any incidental snow excess delays exposure of the bare land or ice underneath, i.e. triggers the albedo feedback. We now present four possible factors or model weaknesses that could underpin this chain of events, leading up to a perennial snow cover in places where it should not exist. The factors / weaknesses are not mutually exclusive and may even be related (e.g. rain and clouds). The aim of this discussion is to improve understanding of our model results on one hand, and to guide future model development and analysis on the other.

First, in regions with little snowfall and melt, erosion and sublimation by blowing snow are two relatively important SMB components. Therefore, even state-of-the-art regional climate models, such as RACMO2, struggle to capture the SMB of the northern GrIS. For example, blowing snow was overestimated in a previous version of RACMO2 (RACMO 2.3p1), causing a too-wide ablation zone in the north (Noël et al., 2018). Here, CESM simulates an ablation zone that is too narrow in all three simulations (Figure 7), which may be explained by the fact that neither drifting snow redistribution, nor drifting snow sublimation are included in CLM (see Equation 1).

Second, along the same reasoning, incidental rainfall could be playing an important role as well. Summer rainfall events add liquid water to the snow pack, thereby speeding up grain growth and thus lowering snow albedo (Oleson, 2013). Moreover, rain water may be refrozen, thereby releasing latent heat into the snow pack and permanently increasing the snow albedo due to the larger snow grain size of refrozen grains (set to 1000 μg in this version of CLM, Oleson (2013)) with respect to fresh snow. As illustrated in Figure 10, CAM-SE currently does not produce the >50 mm accumulated rainfall values over the northern tundras that RACMO2 simulates (panels a and d), with the caveat that RACMO2 rainfall rates have not been validated with station data in this region. Still, we deem it unlikely that CAM-SE simulates realistic rainfall (both intensity and frequency) in this area, and rather underpredicts summer rain by a factor of 2 or more (Figure 10). Further, there seems no significant change in north Greenland rainfall rates in both VR simulations. (panels b and c). This ties in with Bacmeister et al. (2014), who remarked that increasing horizontal resolution by itself does not lead to dramatically improved climate simulations, and must be accompanied by new cloud and convection parametrizations. Existing parameterizations in CAM were developed with specific spatial and temporal scales in mind, and contain assumptions that may break down at higher resolutions (Bacmeister et al., 2014). For completeness, it is remarked that in this version of CESM, precipitation is phase repartitioned by the land component CLM

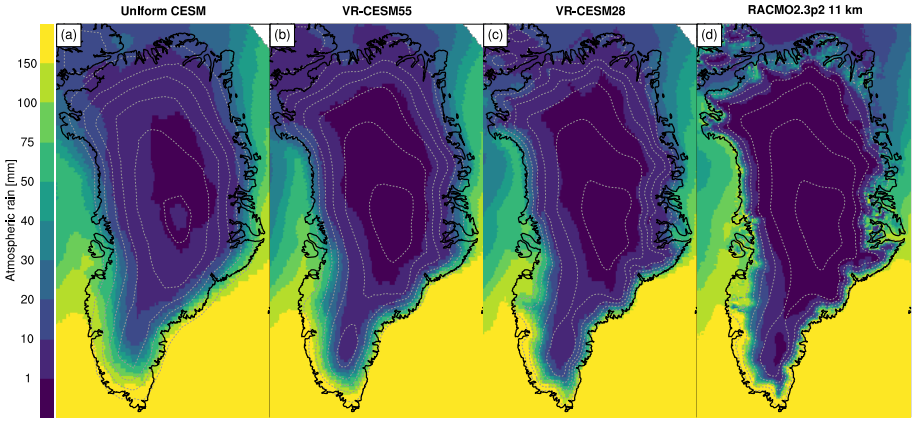

Figure 10. Mean JJA rainfall over the period 1980-1999 in mm as simulated by CAM-SE. RACMO2 data is shown for reference. All three CESM simulations underpredict rain across North Greenland. CESM data have been regridded to a common regular mesh of 0.25° using bi-linear interpolation. Note the non-linear colour scale.

based on the atmospheric surface temperature[2]. We find that summer rainfall rates after repartitioning are markedly higher over specific ablation areas / glaciers, but not over the northern tundra region (not shown). The phase repartitioning model mechanic is therefore not sufficient in compensating for a possible rain bias during summertime.

The third factor, cloud physics, is similar in origin to the previous factor of rainfall. As mentioned earlier, current CAM cloud physics have been developed with specific spatial and temporal resolutions in mind, and are not necessarily performing better on a decreased grid spacing and a smaller physics time step. Moreover, a recent study indicated that CAM5 simulates insufficient cloud cover in summer, especially non-opaque liquid-containing clouds that have a strongly positive cloud radiative effect (Lacour et al., 2018). We believe that summer cloud phase, frequency, and opacity are important metrics to consider in future studies that are set out to resolve the north-Greenland permanent snow bias.

Finally, we propose CLM snow physics as a possible factor or model weakness that could be responsible for reinforcing a positive mass balance. Currently, the CLM snow model operates with a tipping bucket model for liquid water, while maintaining an irreducible water content of 3.3 % (Oleson, 2013). Further, the grain size of refrozen snow is set to 1000 μg. A previous study carried out with RACMO2 indicated that both the irreducible water content and the refreezing grain size are sensitive parameters that impact total melt and runoff generated by the model (van Angelen et al., 2012). It could at some point be worthwhile to explore this avenue of model development in future studies that target Greenland, especially since they are simple parameters to adjust.

[2]CLM5 Technical Note, https://escomp.github.io/ctsm-docs/doc/build/html/tech_note/Ecosystem/CLM50_Tech_Note_Ecosystem.html

5 Summary and Conclusions

For the first time, regionally refined GCM simulations using VR-CESM have been performed at 55 and 28 km over the greater Greenland region to study the impact of spatial resolution on GrIS SMB. Compared to a uniform resolution (1° or ∼111 km) control run, topography is resolved with greater fidelity, leading to improved patterns in orographic precipitation, most notably in southern Greenland and along the western and eastern margins. At the same time, a general drying in the GrIS interior occurs, which substantially improves correlations to IceBridge accumulation radar and in-situ measurements of accumulation. Arguably, VR-CESM performs on-par with RCMs in reproducing these observations, especially at 28 km. GrIS integrated precipitation is reduced from 893 to 745 Gt in VR-CESM28, which is within 6% of a best-estimate RCM figure (707 Gt). The improved distribution of accumulation may prove pivotal in transient simulations, as snowfall modulates the timing and strength of the snow-albedo feedback (Picard et al., 2012) and impacts ice advection.

In the ablation zone, the CESM simulations were evaluated using geographically sparse in-situ measurements. Despite its coarse resolution of ∼111 km, we found that Uniform CESM reproduces these measurements to a reasonable degree, which represents a positive result for CESM at low resolution, suggesting that the subgrid elevation classes are effective (Section 2.3). In both VR-CESM simulations, a positive SMB bias developed in the ablation zone, which signalled an unexpected regression (too little ablation). This was reflected in GrIS-integrated runoff, which was found to be substantially lower in VR-CESM55 and VR-CESM28 compared to Uniform CESM. A basins-by-basin analysis revealed that the largest reductions in runoff are found in the northern and eastern basins, with a good agreement in the other basins. Likely, large-scale circulation changes can be excluded as the prime driving mechanism, as T500 and T700 difference maps indicated no significant cooling over these areas in summer. Instead, we linked the reduction in runoff to clouds, as clouds impact the radiative budget at the surface through the emission of longwave radiation. We highlighted the fact that downwelling longwave radiation is reduced in both VR-CESM simulations, in particular over the regions where runoff decreased with resolution.

At the same time, we could not ignore the outstanding bias in CESM of permanent snow cover over north Greenland peripheral glaciers and tundras. This bias was found to worsen in VR-CESM, rather than improve, leading to more positive surface albedo and a more negative net radiative budget, compared to Uniform CESM. We highlighted four candidate model weaknesses that could be underpinning the bias. With these four factors — blowing snow, rainfall, clouds, snow physics — we provided directions for future studies that are concerned with Greenland. We strongly believe that for GrIS SMB studies, addressing these model weaknesses will prove more important than e.g. increasing the horizontal resolution further, as is done in other studies (Rhoades et al., 2018).

To conclude, our case study demonstrates that VR-CESM is a promising technique for dynamically downscaling GCM climate simulations over an Arctic region, while maintaining model consistency and allowing for feedbacks between the region of interest and the rest of the globe. A finer resolution leads to better resolved storms that are taking different pathways than their low-resolution counterparts, and therefore change precipitation and cloud cover patterns on a local scale. VR-CESM can serve as a tool for modellers that are interested in the dynamical response of the GrIS to future SMB changes, at a reasonable computational cost. At the time this manuscript was written, it was not possible to run VR-CESM in coupled mode with an

active ocean model. Still, high-resolution future projections of GrIS SMB could be generated using VR-CESM when high-frequency output from a fully-coupled scenario simulation is used as a boundary conditions at the sea surface.

Data availability. Climate model data used in our analysis are available on Zenodo, https://doi.org/10.5281/zenodo.2579606

Author contributions. LvK and MRB originally conceived the study. The simulations were set up and carried out by LvK and AMR with help from ARH and CMZ. LvK led the analysis and the writing of the manuscript, with contributions from all the other authors.

Competing interests. The authors declare no competing interests.

Acknowledgements. The authors would like to thank the editor, Xavier Fettweis, and two anonymous referees for their constructive comments. Further, we had fruitful discussions with Paul Ullrich (UC Davis) and Aarnout van Delden (UU/IMAU), and the RACMO2 data was kindly provided by Brice Noël (UU/IMAU). This work was carried out under the program of the Netherlands Earth System Science Centre (NESSC), financially supported by the Ministry of Education, Culture and Science (OCW, Grantnr. 024.002.001). Author Alan Rhoades was funded by the U.S. Department of Energy, Office of Science "An Integrated Evaluation of the Simulated Hydroclimate System of the Continental US" project (award no. DE-SC0016605).

References

Bacmeister, J. T., Wehner, M. F., Neale, R. B., Gettelman, A., Hannay, C., Lauritzen, P. H., Caron, J. M., and Truesdale, J. E.: Exploratory High-Resolution Climate Simulations Using the Community Atmosphere Model (CAM), J. Climate, 27, 3073–3099, https://doi.org/10.1175/JCLI-D-13-00387.1, 2014.

Bales, R. C., Guo, Q., Shen, D., McConnell, J. R., Du, G., Burkhart, J. F., Spikes, V. B., Hanna, E., and Cappelen, J.: Annual Accumulation for Greenland Updated Using Ice Core Data Developed during 2000–2006 and Analysis of Daily Coastal Meteorological Data, Journal of Geophysical Research: Atmospheres, 114, https://doi.org/10.1029/2008JD011208, 2009.

Beljaars, A. C. M., Brown, A. R., and Wood, N.: A New Parametrization of Turbulent Orographic Form Drag, Q.J.R. Meteorol. Soc., 130, 1327–1347, https://doi.org/10.1256/qj.03.73, 2004.

Citterio, M. and Ahlstrøm, A. P.: Brief Communication "The Aerophotogrammetric Map of Greenland Ice Masses", The Cryosphere, 7, 445–449, https://doi.org/10.5194/tc-7-445-2013, 2013.

Cogley, J. G.: Greenland Accumulation: An Error Model, Journal of Geophysical Research: Atmospheres, 109, https://doi.org/10.1029/2003JD004449, 2004.

Cullather, R. I., Nowicki, S. M. J., Zhao, B., and Suarez, M. J.: Evaluation of the Surface Representation of the Greenland Ice Sheet in a General Circulation Model, Journal of Climate, 27, 4835–4856, https://doi.org/10.1175/JCLI-D-13-00635.1, 2014.

Dee, D. P., Uppala, S. M., Simmons, A. J., Berrisford, P., Poli, P., Kobayashi, S., Andrae, U., Balmaseda, M. A., Balsamo, G., Bauer, P., Bechtold, P., Beljaars, A. C. M., van de Berg, L., Bidlot, J., Bormann, N., Delsol, C., Dragani, R., Fuentes, M., Geer, A. J., Haimberger, L., Healy, S. B., Hersbach, H., Hólm, E. V., Isaksen, L., Kållberg, P., Köhler, M., Matricardi, M., McNally, A. P., Monge-Sanz, B. M., Morcrette, J.-J., Park, B.-K., Peubey, C., de Rosnay, P., Tavolato, C., Thépaut, J.-N., and Vitart, F.: The ERA-Interim Reanalysis: Configuration and Performance of the Data Assimilation System, Q.J.R. Meteorol. Soc., 137, 553–597, https://doi.org/10.1002/qj.828, 2011.

Delworth, T. L., Rosati, A., Anderson, W., Adcroft, A. J., Balaji, V., Benson, R., Dixon, K., Griffies, S. M., Lee, H.-C., Pacanowski, R. C., Vecchi, G. A., Wittenberg, A. T., Zeng, F., and Zhang, R.: Simulated Climate and Climate Change in the GFDL CM2.5 High-Resolution Coupled Climate Model, J. Climate, 25, 2755–2781, https://doi.org/10.1175/JCLI-D-11-00316.1, 2011.

Dennis, J. M., Edwards, J., Evans, K. J., Guba, O., Lauritzen, P. H., Mirin, A. A., St-Cyr, A., Taylor, M. A., and Worley, P. H.: CAM-SE: A Scalable Spectral Element Dynamical Core for the Community Atmosphere Model, The International Journal of High Performance Computing Applications, 26, 74–89, https://doi.org/10.1177/1094342011428142, 2012.

Evans, K. J., Lauritzen, P. H., Mishra, S. K., Neale, R. B., Taylor, M. A., and Tribbia, J. J.: AMIP Simulation with the CAM4 Spectral Element Dynamical Core, J. Climate, 26, 689–709, https://doi.org/10.1175/JCLI-D-11-00448.1, 2012.

Evans, K. J., Kennedy, J. H., Lu, D., Forrester, M. M., Price, S., Fyke, J., Bennett, A. R., Hoffman, M. J., Tezaur, I., Zender, C. S., and Vizcaíno, M.: LIVVkit 2.1: Automated and Extensible Ice Sheet Model Validation, Geoscientific Model Development Discussions, pp. 1–31, https://doi.org/10.5194/gmd-2018-70, 2018.

Eyring, V., Bony, S., Meehl, G. A., Senior, C. A., Stevens, B., Stouffer, R. J., and Taylor, K. E.: Overview of the Coupled Model Intercomparison Project Phase 6 (CMIP6) Experimental Design and Organization, Geoscientific Model Development, 9, 1937–1958, https://doi.org/10.5194/gmd-9-1937-2016, 2016.

Fettweis, X., Franco, B., Tedesco, M., van Angelen, J. H., Lenaerts, J. T. M., van den Broeke, M. R., and Gallée, H.: Estimating the Greenland Ice Sheet Surface Mass Balance Contribution to Future Sea Level Rise Using the Regional Atmospheric Climate Model MAR, The Cryosphere, 7, 469–489, https://doi.org/10.5194/tc-7-469-2013, 2013a.

Fettweis, X., Hanna, E., Lang, C., Belleflamme, A., Erpicum, M., and Gallée, H.: Brief Communication "Important Role of the Mid-Tropospheric Atmospheric Circulation in the Recent Surface Melt Increase over the Greenland Ice Sheet", The Cryosphere, 7, 241–248, https://doi.org/10.5194/tc-7-241-2013, 2013b.

Fischer, R., Nowicki, S., Kelley, M., and Schmidt, G.: A System of Conservative Regridding for Ice-Atmosphere Coupling in a General Circulation Model (GCM), Geoscientific Model Development, 7, p. 883–907, https://doi.org/10.5194/gmd-7-883-2014, 2014.

Flanner, M. G. and Zender, C. S.: Snowpack Radiative Heating: Influence on Tibetan Plateau Climate, Geophysical Research Letters, 32, https://doi.org/10.1029/2004GL022076, 2005.

Gates, W. L., Boyle, J. S., Covey, C., Dease, C. G., Doutriaux, C. M., Drach, R. S., Fiorino, M., Gleckler, P. J., Hnilo, J. J., Marlais, S. M., Phillips, T. J., Potter, G. L., Santer, B. D., Sperber, K. R., Taylor, K. E., and Williams, D. N.: An Overview of the Results of the Atmospheric Model Intercomparison Project (AMIP I), Bull. Amer. Meteor. Soc., 80, 29–56, https://doi.org/10.1175/1520-0477(1999)080<0029:AOOTRO>2.0.CO;2, 1999.

Gettelman, A. and Morrison, H.: Advanced Two-Moment Bulk Microphysics for Global Models. Part I: Off-Line Tests and Comparison with Other Schemes, J. Climate, 28, 1268–1287, https://doi.org/10.1175/JCLI-D-14-00102.1, 2014.

Gettelman, A., Callaghan, P., Larson, V. E., Zarzycki, C. M., Bacmeister, J., Lauritzen, P. H., Bogenschutz, P. A., and Neale, R.: Regional Climate Simulations With the Community Earth System Model, Journal of Advances in Modeling Earth Systems, https://doi.org/10.1002/2017MS001227, 2018.

Guba, O., Taylor, M. A., Ullrich, P. A., Overfelt, J. R., and Levy, M. N.: The Spectral Element Method (SEM) on Variable-Resolution Grids: Evaluating Grid Sensitivity and Resolution-Aware Numerical Viscosity, Geosci. Model Dev., 7, 2803–2816, https://doi.org/10.5194/gmd-7-2803-2014, 2014.

Helsen, M. M., van de Wal, R. S. W., Reerink, T. J., Bintanja, R., Madsen, M. S., Yang, S., Li, Q., and Zhang, Q.: On the Importance of the Albedo Parameterization for the Mass Balance of the Greenland Ice Sheet in EC-Earth, The Cryosphere, 11, 1949–1965, https://doi.org/10.5194/tc-11-1949-2017, 2017.

Herrington, A. and Reed, K.: An Idealized Test of the Response of the Community Atmosphere Model to Near-Grid-Scale Forcing Across Hydrostatic Resolutions, Journal of Advances in Modeling Earth Systems, 10, 560–575, https://doi.org/10.1002/2017MS001078, 2018.

Howat, I. M., Negrete, A., and Smith, B. E.: The Greenland Ice Mapping Project (GIMP) Land Classification and Surface Elevation Data Sets, The Cryosphere, 8, 1509–1518, https://doi.org/10.5194/tc-8-1509-2014, 2014.

Huang, X., Rhoades, A. M., Ullrich, P. A., and Zarzycki, C. M.: An Evaluation of the Variable-Resolution CESM for Modeling California's Climate, J. Adv. Model. Earth Syst., 8, 345–369, https://doi.org/10.1002/2015MS000559, 2016.

Hurrell, J. W., Hack, J. J., Shea, D., Caron, J. M., and Rosinski, J.: A New Sea Surface Temperature and Sea Ice Boundary Dataset for the Community Atmosphere Model, J. Climate, 21, 5145–5153, https://doi.org/10.1175/2008JCLI2292.1, 2008.

Kennedy, J. H., Bennett, A. R., Evans, K. J., Price, S., Hoffman, M., Lipscomb, W. H., Fyke, J., Vargo, L., Boghozian, A., Norman, M., and Worley, P. H.: LIVVkit: An Extensible, Python-Based, Land Ice Verification and Validation Toolkit for Ice Sheet Models, Journal of Advances in Modeling Earth Systems, 9, 854–869, https://doi.org/10.1002/2017MS000916, 2017.

Lacour, A., Chepfer, H., Miller, N. B., Shupe, M. D., Noel, V., Fettweis, X., Gallee, H., Kay, J. E., Guzman, R., and Cole, J.: How Well Are Clouds Simulated over Greenland in Climate Models? Consequences for the Surface Cloud Radiative Effect over the Ice Sheet, J. Climate, 31, 9293–9312, https://doi.org/10.1175/JCLI-D-18-0023.1, 2018.

Lauritzen, P. H., Nair, R. D., Herrington, A. R., Callaghan, P., Goldhaber, S., Dennis, J. M., Bacmeister, J. T., Eaton, B. E., Zarzycki, C. M., Taylor, M. A., Ullrich, P. A., Dubos, T., Gettelman, A., Neale, R. B., Dobbins, B., Reed, K. A., Hannay, C., Medeiros, B., Benedict,

J. J., and Tribbia, J. J.: NCAR Release of CAM-SE in CESM2.0: A Reformulation of the Spectral-Element Dynamical Core in Dry-Mass Vertical Coordinates with Comprehensive Treatment of Condensates and Energy, Journal of Advances in Modeling Earth Systems, 0, https://doi.org/10.1029/2017MS001257, 2018.

Lefebre, F., Fettweis, X., Gallée, H., Ypersele, J.-P. V., Marbaix, P., Greuell, W., and Calanca, P.: Evaluation of a High-Resolution Regional Climate Simulation over Greenland, Climate Dynamics, 25, 99–116, https://doi.org/10.1007/s00382-005-0005-8, 2005.

Leguy, G., Lipscomb, W. H., and Sacks, W. J.: CESM Land Ice Documentation and User Guide, https://escomp.github.io/cism-docs/cism-in-cesm/doc_work/html/, 2018.

Lenaerts, J. T., Vizcaino, M., Fyke, J., van Kampenhout, L., and van den Broeke, M. R.: Present-Day and Future Antarctic Ice Sheet Climate and Surface Mass Balance in the Community Earth System Model, Climate Dynamics, 47, 1367–1381, 2016.

Lewis, G., Osterberg, E., Hawley, R., Whitmore, B., and Marshall, H. P.: Regional Greenland Accumulation Variability from Operation IceBridge Airborne Accumulation Radar, The Cryosphere Discussions, pp. 1–29, https://doi.org/10.5194/tc-2016-248, 2016.

Ligtenberg, S. R. M., Kuipers Munneke, P., Noël, B. P. Y., and van den Broeke, M. R.: Brief Communication: Improved Simulation of the Present-Day Greenland Firn Layer (1960–2016), The Cryosphere, 12, 1643–1649, https://doi.org/10.5194/tc-12-1643-2018, 2018.

Lipscomb, W. H., Fyke, J. G., Vizcaíno, M., Sacks, W. J., Wolfe, J., Vertenstein, M., Craig, A., Kluzek, E., and Lawrence, D. M.: Implementation and Initial Evaluation of the Glimmer Community Ice Sheet Model in the Community Earth System Model, Journal of Climate, 26, 7352–7371, https://doi.org/10.1175/JCLI-D-12-00557.1, 2013.

Machguth, H., Thomsen, H. H., Weidick, A., Ahlstrøm, A. P., Abermann, J., Andersen, M. L., Andersen, S. B., Bjørk, A. A., Box, J. E., Braithwaite, R. J., Bøggild, C. E., Citterio, M., Clement, P., Colgan, W., Fausto, R. S., Gleie, K., Gubler, S., Hasholt, B., Hynek, B., Knudsen, N. T., Larsen, S. H., Mernild, S. H., Oerlemans, J., Oerter, H., Olesen, O. B., Smeets, C. J. P. P., Steffen, K., Stober, M., Sugiyama, S., As, D. V., Broeke, M. R. V. D., and Wal, R. S. W. V. D.: Greenland Surface Mass-Balance Observations from the Ice-Sheet Ablation Area and Local Glaciers, Journal of Glaciology, 62, 861–887, https://doi.org/10.1017/jog.2016.75, 2016.

Matte, D., Laprise, R., Thériault, J. M., and Lucas-Picher, P.: Spatial Spin-up of Fine Scales in a Regional Climate Model Simulation Driven by Low-Resolution Boundary Conditions, Clim Dyn, 49, 563–574, https://doi.org/10.1007/s00382-016-3358-2, 2017.

Molod, A., Takacs, L., Suarez, M., and Bacmeister, J.: Development of the GEOS-5 Atmospheric General Circulation Model: Evolution from MERRA to MERRA2, Geosci. Model Dev., 8, 1339–1356, https://doi.org/10.5194/gmd-8-1339-2015, 2015.

Mottram, R., Boberg, F., Langen, P., Yang, S., Rodehacke, C., Christensen, J. H., and Madsen, M. S.: Surface Mass Balance of the Greenland Ice Sheet in the Regional Climate Model HIRHAM5: Present State and Future Prospects, p. 12, 2017.

Müller, W. A., Jungclaus, J. H., Mauritsen, T., Baehr, J., Bittner, M., Budich, R., Bunzel, F., Esch, M., Ghosh, R., Haak, H., Ilyina, T., Kleine, T., Kornblueh, L., Li, H., Modali, K., Notz, D., Pohlmann, H., Roeckner, E., Stemmler, I., Tian, F., and Marotzke, J.: A Higher-Resolution Version of the Max Planck Institute Earth System Model (MPI-ESM1.2-HR), Journal of Advances in Modeling Earth Systems, 0, https://doi.org/10.1029/2017MS001217, 2018.

Neale, R. B., Chen, C.-C., Gettelman, A., Lauritzen, P. H., Park, S., Williamson, D. L., Conley, A. J., Garcia, R., Kinnison, D., and Lamarque, J.-F.: Description of the NCAR Community Atmosphere Model (CAM 5.0), NCAR Tech. Note NCAR/TN-486+ STR, 2012.

Noël, B., van de Berg, W. J., van Meijgaard, E., Kuipers Munneke, P., van de Wal, R. S. W., and van den Broeke, M. R.: Evaluation of the Updated Regional Climate Model RACMO2.3: Summer Snowfall Impact on the Greenland Ice Sheet, The Cryosphere, 9, 1831–1844, https://doi.org/10.5194/tc-9-1831-2015, 2015.

Noël, B., van de Berg, W. J., Machguth, H., Lhermitte, S., Howat, I., Fettweis, X., and van den Broeke, M. R.: A Daily, 1 Km Resolution Data Set of Downscaled Greenland Ice Sheet Surface Mass Balance (1958–2015), The Cryosphere, 10, 2361–2377, https://doi.org/10.5194/tc-10-2361-2016, 2016.

Noël, B., van de Berg, W. J., van Wessem, J. M., van Meijgaard, E., van As, D., Lenaerts, J. T. M., Lhermitte, S., Kuipers Munneke, P., Smeets, C. J. P. P., van Ulft, L. H., van de Wal, R. S. W., and van den Broeke, M. R.: Modelling the Climate and Surface Mass Balance of Polar Ice Sheets Using RACMO2 – Part 1: Greenland (1958–2016), The Cryosphere, 12, 811–831, https://doi.org/10.5194/tc-12-811-2018, 2018.

Oleson, K. W.: Technical Description of Version 4.5 of the Community Land Model (CLM), NCAR Technical Note NCAR/TN-503+ STR, National Center for Atmospheric Research, Boulder, CO, 2013.

Picard, G., Domine, F., Krinner, G., Arnaud, L., and Lefebvre, E.: Inhibition of the Positive Snow-Albedo Feedback by Precipitation in Interior Antarctica, Nature Climate Change, 2, 795–798, https://doi.org/10.1038/nclimate1590, 2012.

Pollard, D.: A Retrospective Look at Coupled Ice Sheet–Climate Modeling, Climatic Change, 100, 173–194, https://doi.org/10.1007/s10584-010-9830-9, 2010.

Punge, H. J., Gallée, H., Kageyama, M., and Krinner, G.: Modelling Snow Accumulation on Greenland in Eemian, Glacial Inception, and Modern Climates in a GCM, Climate of the Past, 8, 1801– 1819, https://doi.org/10.5194/cp-8-1801-2012, 2012.

Rae, J. G. L., Aðalgeirsdóttir, G., Edwards, T. L., Fettweis, X., Gregory, J. M., Hewitt, H. T., Lowe, J. A., Lucas-Picher, b., Mottram, R. H., Payne, A. J., Ridley, J. K., Shannon, S. R., van de Berg, W. J., van de Wal, R. S. W., and van den Broeke, M. R.: Greenland Ice Sheet Surface Mass Balance: Evaluating Simulations and Making Projections with Regional Climate Models, The Cryosphere, 6, 1275–1294, https://doi.org/10.5194/tc-6-1275-2012, 2012.

Rhoades, A. M., Huang, X., Ullrich, P. A., and Zarzycki, C. M.: Characterizing Sierra Nevada Snowpack Using Variable-Resolution CESM, J. Appl. Meteor. Climatol., 55, 173–196, https://doi.org/10.1175/JAMC-D-15-0156.1, 2015.

Rhoades, A. M., Ullrich, P. A., and Zarzycki, C. M.: Projecting 21st Century Snowpack Trends in Western USA Mountains Using Variable-Resolution CESM, Clim Dyn, pp. 1–28, https://doi.org/10.1007/s00382-017-3606-0, 2017.

Rhoades, A. M., Ullrich, P. A., Zarzycki, C. M., Johansen, H., Margulis, S. A., Morrison, H., Xu, Z., and Collins, W.: Sensitivity of Mountain Hydroclimate Simulations in Variable-Resolution CESM to Microphysics and Horizontal Resolution, Journal of Advances in Modeling Earth Systems, https://doi.org/10.1029/2018MS001326, 2018.

Rignot, E. and Mouginot, J.: Ice Flow in Greenland for the International Polar Year 2008–2009, Geophysical Research Letters, 39, https://doi.org/10.1029/2012GL051634, 2012.

Shannon, S., Smith, R., Wiltshire, A., Payne, T., Huss, M., Betts, R., Caesar, J., Koutroulis, A., Jones, D., and Harrison, S.: Global Glacier Volume Projections under High-End Climate Change Scenarios, The Cryosphere, 13, 325–350, https://doi.org/https://doi.org/10.5194/tc-13-325-2019, 2019.

Small, R. J., Bacmeister, J., Bailey, D., Baker, A., Bishop, S., Bryan, F., Caron, J., Dennis, J., Gent, P., Hsu, H.-m., Jochum, M., Lawrence, D., Muñoz, E., diNezio, P., Scheitlin, T., Tomas, R., Tribbia, J., Tseng, Y.-h., and Vertenstein, M.: A New Synoptic Scale Resolving Global Climate Simulation Using the Community Earth System Model, Journal of Advances in Modeling Earth Systems, 6, 1065–1094, https://doi.org/10.1002/2014MS000363, 2014.

Sodemann, H., Schwierz, C., and Wernli, H.: Interannual Variability of Greenland Winter Precipitation Sources: Lagrangian Moisture Diagnostic and North Atlantic Oscillation Influence, Journal of Geophysical Research: Atmospheres, 113, https://doi.org/10.1029/2007JD008503, 2008.

Swenson, S. C. and Lawrence, D. M.: A New Fractional Snow-Covered Area Parameterization for the Community Land Model and Its Effect on the Surface Energy Balance, Journal of Geophysical Research: Atmospheres, 117, https://doi.org/10.1029/2012JD018178, 2012.

Ullrich, P. A.: SQuadGen: Spherical Quadrilateral Grid Generator, 2014.

van Angelen, J. H., Lenaerts, J. T. M., Lhermitte, S., Fettweis, X., Kuipers Munneke, P., van den Broeke, M. R., van Meijgaard, E., and Smeets, C. J. P. P.: Sensitivity of Greenland Ice Sheet Surface Mass Balance to Surface Albedo Parameterization: A Study with a Regional Climate Model, The Cryosphere, 6, 1175–1186, https://doi.org/10.5194/tc-6-1175-2012, 2012.

van Angelen, J. H., M. Lenaerts, J. T., van den Broeke, M. R., Fettweis, X., and van Meijgaard, E.: Rapid Loss of Firn Pore Space Accelerates 21st Century Greenland Mass Loss, Geophys. Res. Lett., 40, 2109–2113, https://doi.org/10.1002/grl.50490, 2013.

van den Broeke, M. R., Enderlin, E. M., Howat, I. M., Kuipers Munneke, P., Noël, B. P. Y., van de Berg, W. J., van Meijgaard, E., and Wouters, B.: On the Recent Contribution of the Greenland Ice Sheet to Sea Level Change, The Cryosphere, 10, 1933–1946, https://doi.org/10.5194/tc-10-1933-2016, 2016.

van Kampenhout, L., Lenaerts, J. T. M., Lipscomb, W. H., Sacks, W. J., Lawrence, D. M., Slater, A. G., and van den Broeke, M. R.: Improving the Representation of Polar Snow and Firn in the Community Earth System Model, J. Adv. Model. Earth Syst., 9, 2583–2600, https://doi.org/10.1002/2017MS000988, 2017.

Van Tricht, K., Lhermitte, S., Gorodetskaya, I. V., and van Lipzig, N. P. M.: Improving Satellite-Retrieved Surface Radiative Fluxes in Polar Regions Using a Smart Sampling Approach, The Cryosphere, 10, 2379–2397, https://doi.org/10.5194/tc-10-2379-2016, 2016.

Vizcaíno, M., Lipscomb, W. H., Sacks, W. J., van Angelen, J. H., Wouters, B., and van den Broeke, M. R.: Greenland Surface Mass Balance as Simulated by the Community Earth System Model. Part I: Model Evaluation and 1850–2005 Results, Journal of Climate, 26, 7793–7812, https://doi.org/10.1175/JCLI-D-12-00615.1, 2013.

Wehner, M. F., Reed, K. A., Li, F., Prabhat, Bacmeister, J., Chen, C.-T., Paciorek, C., Gleckler, P. J., Sperber, K. R., Collins, W. D., Gettelman, A., and Jablonowski, C.: The Effect of Horizontal Resolution on Simulation Quality in the Community Atmospheric Model, CAM5.1, J. Adv. Model. Earth Syst., 6, 980–997, https://doi.org/10.1002/2013MS000276, 2014.

Zarzycki, C. M. and Jablonowski, C.: A Multidecadal Simulation of Atlantic Tropical Cyclones Using a Variable-Resolution Global Atmospheric General Circulation Model, J. Adv. Model. Earth Syst., 6, 805–828, https://doi.org/10.1002/2014MS000352, 2014.

Zarzycki, C. M., Levy, M. N., Jablonowski, C., Overfelt, J. R., Taylor, M. A., and Ullrich, P. A.: Aquaplanet Experiments Using CAM's Variable-Resolution Dynamical Core, Journal of Climate, 27, 5481–5503, https://doi.org/10.1175/JCLI-D-14-00004.1, 2014.

Zarzycki, C. M., Jablonowski, C., Thatcher, D. R., and Taylor, M. A.: Effects of Localized Grid Refinement on the General Circulation and Climatology in the Community Atmosphere Model, J. Climate, 28, 2777–2803, https://doi.org/10.1175/JCLI-D-14-00599.1, 2015.

Ziemen, F., Rodehacke, C., and Mikolajewicz, U.: Coupled Ice Sheet–Climate Modeling under Glacial and Pre-Industrial Boundary Conditions, Climate of the Past, 10, 1817–1836, https://doi.org/10.5194/cp-10-1817-2014, 2014.